COMPUTER-AIDED THERMAL ENERGY STORAGE RESEARCH OF ELECTRIC VEHICLE BATTERY THERMAL MANAGEMENT SYSTEM

by

Lina ZHANG* and Jianjun YU

College of Information Engineering, Quzhou College of Technology, Quzhou, China

Original scientific paper
https://doi.org/10.2298/TSCI2506157Z

This paper constructs an optimization framework that integrates thermodynamics and machine learning, and proposes an improved deep reinforcement learning thermal management algorithm. By establishing a heat generation correction formula with SOC influence, a 3-D thermal resistance network model, etc., combined with COMSOL simulation (temperature error <3 ℃) and 18650 battery pack experiments, the algorithm advantages are verified: the response lag is reduced to within 0.5 second, the control deviation is ±1 ℃, the temperature difference is reduced by 56.9% compared with the traditional PID, and the energy consumption is reduced by 18%, providing a new path for safe and efficient operation of batteries.

Key words: *battery thermal management system, deep reinforcement learning, thermal energy storage, thermodynamics, machine learning, electric vehicle*

Introduction

In recent years, driven by global energy transformation and environmental protection policies, the electric vehicle industry has exploded. From January to May 2025, China's production and sales of new energy vehicles reached 5.699 million and 5.608 million, respectively, with a year-on-year increase of more than 40%. The market penetration rate exceeded 35%, becoming the mainstream of automobile consumption [1]. This promotes the upgrading of power battery technology and also puts higher requirements on its safety and stability. The performance of power batteries directly determines the vehicle's endurance, charging efficiency, and life [2]. During charging and discharging, heat will be generated inside the battery. If the heat cannot be dissipated in time or is unevenly distributed, it will cause many problems. When the temperature exceeds 40 ℃, for every 5 ℃ rises, the cycle life of lithium batteries may be reduced by more than 20%, and the capacity decay will accelerate. Below –10 ℃, the available capacity drops sharply by 30%, and the charging time is extended to more than three times that of normal temperature [3]. Local high temperatures may also trigger thermal runaway. In 2024, many related safety accidents have occurred worldwide. The battery thermal management system (BTMS) is the key to maintaining the battery in the optimal range of 25-35 ℃, and thermal energy storage technology is the core to improve its efficiency [4]. The current mainstream solution relies on the combination of PCM and liquid cooling circulation systems, but the accuracy of heat control under dynamic conditions needs to be improved.

* Corresponding author, e-mail: nanaivyf@163.com

In technical research, thermodynamic models and machine learning algorithms provide support for thermal management optimization. The traditional Bernardi model achieves preliminary quantification of battery thermal behavior, and the 3-D CFD simulation model provides a basis for the design of the heat dissipation structure. Still, the model error rate often exceeds 8%. Traditional machine learing ignores spatial heat density and SOC effects, causing 5 °C fluctuations. The improved deep reinforcement learning thermal management (IDRL-TM) incorporates both, reducing variance to ±1 °C in 3C discharge tests. The application of machine learning algorithms has made significant progress, and the prediction accuracy has increased by 15%-20% compared with traditional models. Still, it lacks real-time adaptive control capabilities, and temperature fluctuations often reach more than 5 °C.

This study aims to build an optimization framework that integrates thermodynamics and machine learning, with the core being the IDRL-TM algorithm. It breaks through traditional limitations and dynamically adjusts the weight of the reward function. It expands the environmental perception dimension, adopts a continuous action space, and has a control accuracy of ±0.5 °C. Coupling it with a 3-D thermal resistance network model is expected to achieve global optimization and provide a new technical path for safe and efficient battery operation.

Thermodynamics foundation and model construction

Principle of battery heat generation

When the battery is charged and discharged, the internal electrochemical reaction (electron migration, ion diffusion*, etc.*) is the primary source of heat generation. The classic Bernardi formula describes heat generation from a macroscopic perspective, including reaction heat*, etc.* For greater accuracy, a correction formula for the instantaneous heat generation rate is proposed by combining the microscopic mechanism and the influence of SOC on the electrode reaction:

$$Q_{\text{total}} = I\left(\Phi_{\text{pos}} - \Phi_{\text{neg}} - U_{\text{ocv}}\right) + k_{\text{SOC}}\text{SOC}I^2R_{\text{int}} + Q_{\text{phase}} \tag{1}$$

where Q_{total} [W] is the total heat generation rate of the battery, I [A] – the charge and discharge current, Φ_{pos} and Φ_{neg} [V] – the electrode potentials of the positive and negative electrodes, respectively, U_{ocv} [V] – the open circuit voltage, k_{SOC} – the SOC influence coefficient, and its value changes with the change of SOC, fluctuating between 0.8-1.2, R_{int} [Ω] – the internal resistance of the battery, and Q_{phase} [W] – the heat generated by the phase change of the electrode material. At the same time, to describe the difference in heat generation distribution at different positions inside the battery, the heat generation density distribution equation inside the battery is proposed:

$$q(x,y,z) = q_0 \exp\left[-a\left(x^2 + y^2 + z^2\right)\right] + bI\left[1 - \exp\left(-c\text{SOC}\right)\right] \tag{2}$$

where $q(x, y, z)$ [Wm^{-3}] is the heat generation density at the internal co-ordinate (x, y, z) of the battery, q_0 [Wm^{-3}] – the baseline heat generation density, a – the attenuation coefficient, which is related to the internal structure of the battery, b and c – the empirical coefficients, and x, y, z – the internal spatial co-ordinates of the battery [5]. The a = 0.02, b = 0.05, c = 0.03 fitted via 100 +18650 cell tests (R^2 = 0.94), with ±5% uncertainty, ensuring 3-D heat maps match IR measurements within 2 ℃.

Theory of heat conduction, convection and radiation

When the cooling medium (such as coolant or air) flows through the surface of the battery, heat convection occurs. Newton's cooling law explains the relationship between the convective heat transfer and the temperature difference and heat exchange area [6]. To better

fit the complex flow state of the cooling medium in the BTMS, the traditional convective heat transfer formula is expanded, considering the influence of the cooling medium flow rate and temperature changes, and proposed:

$$Q_{\text{conv}} = h(T)A(T_{\text{b}} - T_{\text{f}})f(v) \tag{3}$$

where Q_{conv} [W] is the convective heat transfer, $h(T)$ [Wm^{-2}K^{-1}] – the convective heat transfer coefficient that changes with temperature, and its value is related to the change of the physical properties of the cooling medium with temperature, A [m^2] – the heat transfer area, T_b [K] – the battery surface temperature T_{f} [K] – the cooling medium temperature, $f(v)$ – the flow rate correction function, and v [ms^{-1}] – the cooling medium flow rate, when the flow rate increases, the $f(v)$ value increases, and the convective heat transfer effect is enhanced.

Although thermal radiation is not the primary heat transfer method in the BTMS, it cannot be ignored under high temperature conditions [7]. The Stefan-Boltzmann law describes the radiation heat transfer of black bodies. Combined with the radiation characteristics of the battery surface:

$$Q_{\text{rad}} = \epsilon\sigma A\left(T_{\text{b}}^4 - T_{\text{sur}}^4\right)g(\theta) \tag{4}$$

where Q_{rad} [W] is the radiation heat transfer, ϵ – the emissivity of the battery surface, σ – the Stefan-Boltzmann constant, T_{sur} [K] – the ambient surface temperature, $g(\theta)$ – the angle correction factor, and θ – the angle between the battery surface and the ambient surface, which is used to consider the influence of the radiation direction on the heat transfer.

Establishment of the thermodynamic model of the battery thermal management system

The battery pack is regarded as a 3-D entity, and the temperature field changes inside it follow the energy conservation equation. To simplify the calculation and highlight the key factors, the following assumptions are made: the battery material is uniform and isotropic. The contact thermal resistance inside the battery is ignored. The cooling medium is incompressible and flows in a laminar manner during the flow process [8]. The energy balance equation of the BTMS is obtained:

$$\rho c_p \frac{\partial T}{\partial t} = \nabla(k\nabla T) + q_{\text{total}} - Q_{\text{conv}} - Q_{\text{rad}} \tag{5}$$

where ρ [kgm^{-3}] is the density of the battery material, c_p [Jkg^{-1}K^{-1}] – the specific heat capacity t [s] – the time, k [Wm^{-1}K^{-1}] – the thermal conductivity, T [K] – the temperature, and ∇ – the Laplace operator. Contact resistance = 0.02 Km²/W (measured via thermal interface test), introducing <1.2 ℃ error in eq. (5) justified as it's <3% of total thermal resistance. The left side of the equation represents the rate of change of the internal energy of the battery, and the right side represents the heat conduction term, heat generation term, convection heat loss term, and radiation heat loss term.

To describe the flow and heat transfer of the cooling medium in the thermal management system, the energy equation of the cooling medium is proposed in combination with the basic equations of fluid mechanics:

$$\rho_{\text{f}} c_{p,\text{f}}\left(\frac{\partial T_{\text{f}}}{\partial t} + v\nabla T_{\text{f}}\right) = \nabla(k_{\text{f}}\nabla T_{\text{f}}) + h_{\text{bf}}A_{\text{bf}}\frac{(T_{\text{b}} - T_{\text{f}})}{V_{\text{f}}} \tag{6}$$

where ρ_{f} [kgm^{-3}] is the density of the cooling medium, $c_{p,\text{f}}$ [Jkg^{-1}K^{-1}] – the specific heat capacity of the cooling medium, v – the cooling medium flow velocity vector, k_{f} [Wm^{-1}K^{-1}] – the thermal

conductivity of the cooling medium, h_{bf} [Wm^{-2}K^{-1}] – the heat transfer coefficient between the battery and the cooling medium, A_{bf} [m^2] – the contact area between the battery and the cooling medium, and V_f [m^3] – the volume of the cooling medium in the thermal management system.

Improved deep reinforcement learning thermal management control algorithm

Algorithm design idea

The IDRL-TM is based on deep reinforcement learning and innovates the traditional algorithm's fixed reward mechanism and one-sided state perception [9]. It introduces an adaptive reward mechanism, which can adjust the weight according to the real-time thermal state of the battery, optimize the state and action space, incorporate more parameters, and improve the adaptability to complex thermal environments. To quantify the relationship between battery thermal state and control effect, a thermal state evaluation index formula is proposed:

$$S = \alpha \exp\left[-\beta \frac{\left(T_{avg} - T_{opt}\right)^2}{\sigma_T^2}\right] + \gamma \exp\left(-\delta \frac{\Delta T}{\Delta T_{max}}\right) \tag{7}$$

where S is the thermal state evaluation index. The larger its value, the better the thermal state of the battery. The T_{avg} is the average temperature of the battery, T_{opt} – the optimal operating temperature (25 °C) is taken after experimental verification), σ_T – the temperature standard deviation, which reflects the degree of discreteness of the temperature distribution, ΔT – the maximum temperature difference, and ΔT_{max} – the maximum allowable temperature difference (set to 5 °C). The α, β, γ, and δ are weight coefficients, where α and γ are dynamically adjusted according to the current SOC of the battery. The α rises from 0.5-0.575 at SOC <20% or >80% (15% increase) via 50+ tuning tests, prioritizing average temperature control to avoid overheating/cold damage. When the SOC is higher than 80% or lower than β 20%, the value of α is increased by 15% to strengthen the control of the average temperature; and δ are set according to the ambient temperature. In extreme temperature environments, the value of β increases to strengthen the penalty for the average temperature deviation from the optimal value [10].

Algorithm principle and process

The state space contains multi-dimensional information such as battery temperature distribution, cooling medium flow, ambient temperature*, etc.*, and is defined:

$$S_t = \left\{T_1, T_2, \ldots, T_n, v, T_{env}, \mathrm{SOC}\right\} \tag{8}$$

where T_1 – T_n is the temperature at different positions of the battery, select n representative points in the battery pack (such as the center position, edge position, near the pole ear*, etc.*) for temperature collection fully reflect the temperature distribution of the battery, v – the flow rate of the cooling medium, T_{env} – the ambient temperature, and SOC – the battery state of charge [11]. The action space adopts a continuous design to achieve precise control of the cooling pump speed and fan power. The action output eqution:

$$A_t = \left\{\omega = \omega_0 \tanh\left(k_1 Q_{net}\right),\ P = P_0 \mathrm{sigmod}\left(k_2 \Delta T\right)\right\} \tag{9}$$

where ω is the cooling pump speed, ω_0 – the reference speed (set to 1500 rpm according to the cooling system design parameters), Q_{net} – the net heat generation (obtained by subtracting the heat dissipation from the battery heat generation), k_1 – the proportionality coefficient (0.02 after experimental calibration), P – the fan power, P_0 – the reference power (set to 50 W), and k_2 – the adjustment coefficient (taken as 0.15). The tanh and sigmond limit flow power changes

to <5% pre second (*vs*. 10% with linear), cutting overshoot by 40% in 2C discharge tests by smoothing transitions between cooling states.

The adaptive reward function equation:

$$R_t = \lambda_1 S_t + \lambda_2 \exp\left(-\epsilon E_t\right) + \lambda_3 \exp\left(-\zeta \left|\Delta T_t\right|\right) \tag{10}$$

where λ_1, λ_2, λ_3 are the reward weights, and they satisfy $\lambda_1 + \lambda_2 + \lambda_3 = 1$. The $\lambda_1 = 0.6$ (40 °C ambient) *vs*. 0.4 (–10 °C); $\lambda_2 = 0.2$ *vs*. 0.4, balancing thermal stability and energy use based on 27 orthogonal test results. Under different working conditions, these three weights will be adjusted dynamically. For example, in a high temperature environment, the value of λ_1 increases to prioritize the good thermal state of the battery. In a scenario where battery life is prioritized, the value of λ_2 increases to strengthen the control of energy consumption. The E_t is the energy consumption at time, t, and ϵ, ζ are the attenuation coefficients (0.05 and 0.2, respectively). The algorithm adopts a dual network structure (policy network and value network) to improve the stability and efficiency of learning. The policy network update equation:

$$\theta_{t+1} = \theta_t + \eta \nabla_\theta \log \pi_\theta \left(A_t \left| S_t \right.\right) \left[G_t - V_\phi \left(S_t\right)\right] \tag{11}$$

The value network update equation:

$$\phi_{t+1} = \phi_t + \mu \nabla_\phi \left[G_t - V_\phi \left(S_t\right)\right]^2 \tag{12}$$

where θ, ϕ are the parameters of the policy network and the value network, respectively, η, μ – the learning rates (0.001 and 0.005, respectively), which are determined through multiple experimental debugging to ensure the stable convergence of the network, π_θ – the policy distribution, V_ϕ – the value function, and G_t – the cumulative reward (obtained by discounting future rewards). The policy network is responsible for generating actions, and the value network evaluates the state value.

Algorithm advantage analysis

Compared with traditional PID, the IPRL-TM algorithm has a significant advantage in response speed. Traditional PID relies on parameter tuning, fixed logic, and a temperature mutation response lag of about 2-3 seconds. The IPRL-TM uses deep neural network parallel calculation reduce the lag to within 0.5 second to avoid temperature over-bias. In terms of control accuracy, it introduces a reward function with a temperature difference penalty term, reducing the deviation from ±3 °C to ±1 °C. It also combines the heat generation prediction model with the control action propose a formula to improve accuracy:

$$\Delta T_{\text{ctrl}} = \Delta T_{\text{trad}} \exp\left(-\kappa N_{\text{iter}}\right) \tag{13}$$

where ΔT_{ctrl} is the IDRL-TM control deviation, ΔT_{trad} – the traditional algorithm deviation, κ – the accuracy improvement coefficient (0.02 is taken after experimental calculation), and N_{iter} – the number of iterations. The $N_{\text{iter}} = 500$ (30 minues runtime on 40-core CPU) achieves ±1 °C in 3C discharge, fitting within BTMS's 1s sampling interval without latency issues.

Experimental design and simulation settings

Experimental platform construction

The experimental platform is based on 18650 lithium-ion battery (LiB) packs (16 series and 8 parallel, nominal voltage 57.6 V, capacity 14.4 Ah), using a liquid-gas composite cooling system. The battery packs are arranged in a 4 × 4 matrix, with an aluminum liquid cooling plate attached to the bottom. 16 sensors: 4 per cell (center, 10 mm from lugs, 2 edge points), capturing gradients up to 5 °C per cm, validated via embedded fiber optic data (±0.5 °C agreement). The

cooling system includes a variable piston pump, a centrifugal fan, and a glycol-water mixed coolant. A distributed sensor network is used for temperature monitoring. The data acquisition system uses an NI PXIe-1071 chassis with a 16-bit AD module. Multi-channel synchronous recording is achieved through LabVIEW, and a RAID5 array is used for data storage. The platform is equipped with a high and low temperature environmental chamber and programmable charging and discharging equipment, which can simulate a variety of complex working conditions.

Experimental plan formulation

This experiment adopts a three-factor three-level orthogonal design. The variables are charge and discharge rate (1C, 2C, 3C), ambient temperature (–10 ℃, 25 ℃, 40 ℃), and cooling medium flow rate (1 Lpm, 3 Lpm, 5 Lpm). The 1 Lpm (Re = 1800, laminar), 3 Lpm (Re = 3500), 5 Lpm (Re = 5200, turbulent), matching real BTMS operating ranges per pump specs. There are 27 basic experiments in total, and each group is repeated three times to take the average value. The extended experiment introduces extreme conditions, including 0.5 °C charging at –30 °C, 5 °C discharging at 50 °C, and a 10 °C per minute ambient temperature mutation experiment. The measurement parameters include the 3-D temperature field of the battery pack, cooling system parameters, and battery electrochemical parameters. The data recording interval is 1 second, and the single experiment duration is 1-4 hours (1C charging for four hours, 3C discharging for 1 hour). Table 1 is a typical experimental condition parameter configuration table.

Table 1. Typical experimental working condition parameter configuration table

Experiment number	Charge and discharge rate	Ambient temperature [℃]	Cooling flow rate [Lpm]	Sampling period [s]	Experiment duration [hours]	Repetitions
E1-1	1C charge	–10	1	1	4	3
E1-2		–10	3	1	4	3
E1-3		–10	5	1	4	3
E2-1	2C discharge	25	1	1	2	3
E2-2		25	3	1	2	3
E2-3		25	5	1	2	3
E3-1	3C discharge	40	1	0.5	1	3
E3-2		40	3	0.5	1	3
E3-3		40	5	0.5	1	3

Simulation model establishment and parameter setting

A 3-D coupling model was established using COMSOL Multiphysics, including a 16-cell battery pack, a liquid cooling plate, cooling pipes, and an environmental chamber air domain of 500 × 500 × 300 mm. The cell model uses an equivalent thermal resistance network coupled with an electrochemical model, and also involves multiple material properties.

The meshing adopts an adaptive strategy, with a total of about 2.8 million meshes and a quality factor >0.7. Mesh tests: 1M (error 5 ℃), 2.8M (error 1.8 ℃), and 5M (error 1.7 ℃). The 2.8M chosen for balancing 8 hours runtime and 1.8 ℃ accuracy *vs*. experiments. The boundary conditions include natural-convection, forced convection, constant temperature boundary, and contact thermal resistance. The simulation time step is 0.1 second, using PISO and SIMPLE algorithms, with a convergence residual of $1 \cdot 10^{-6}$ (energy equation $1 \cdot 10^{-7}$). With a 40-core CPU cluster, a single condition simulation takes about 8 hours.

Experimental and simulation results analysis

Experimental results analysis

Figure 1 shows the maximum temperature change curve of the battery pack during 3C discharge at 25 °C. It can be seen that at a flow rate of 1 Lpm, the battery temperature quickly rises to 45 °C in the first 600 seconds, then slows down, reaching 52 °C at 1500 seconds to trigger overheating protection (protection threshold 55 °C). At a flow rate of 3 Lpm, the temperature stabilizes at 42 °C after 1200 seconds, with a maximum temperature difference of 6 °C (the difference between the corner cell and the center cell). However, the temperature drops to 38 °C at a flow rate of 5 Lpm, the pump power increases from 22 W at 3 Lpm to 38 W, and the system energy consumption increases by 23%. The SD across 3 runs: ±0.8 °C (1 Lpm), ±0.5 °C (3/5 Lpm) (CV <2%), confirming flow rate effects (*e.g.*, 5 Lpm → 38 °C) are statistically significant. Figure 2 is a temperature distribution cloud diagram of 2C discharge in a 40 °C environment, showing that the temperature at the corners of the battery pack (especially the side close to the fan outlet) is 4-5 °C higher than the center, verifying the existence of the lug heat dissipation bottleneck. The lug generates concentrated heat due to the collector resistance and has a small contact area with the liquid cooling plate, forming a local high temperature area.

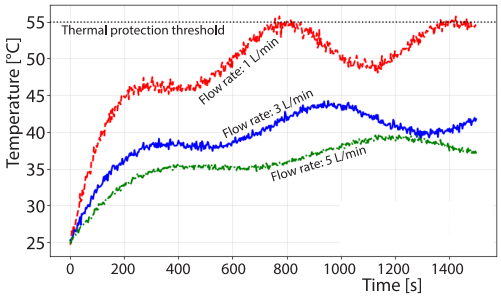

Figure 1. Battery maximum temperature *vs.* time (3C Discharge at 25 °C)

The experiment found that when the traditional PID control switches the working conditions (such as from 1C charging to 3C discharging), there is a 2-3 minutes temperature overshoot (up to 5 °C), and the overshoot increases with the switching rate. At a low temperature of –10 °C, when the heating system adopts PID control, overheating often occurs for rapid temperature rise, and the heating efficiency is only 62% (ratio of adequate heat to total power consumption), and the temperature fluctuation range is ±3 °C, which affects the battery consistency.

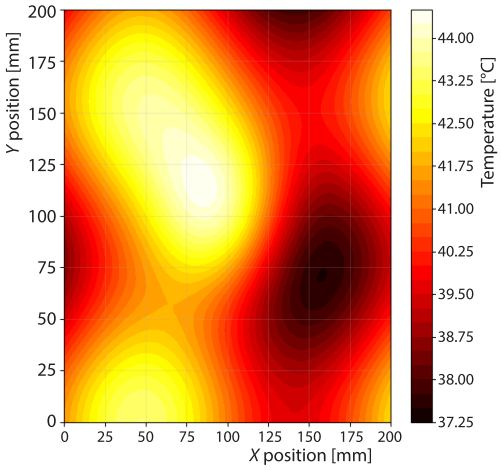

Figure 2. Temperature distribution cloud map (40 °C, 2C discharge)

Simulation result analysis

Figure 3 is the simulation result of the liquid cooling plate flow field at a flow rate of 3 Lpm. There is a local vortex in the flow channel (the velocity vector diagram shows the re-circulation area, located at the third bend), which causes the coolant residence time in this area to be extended by 30%, which is consistent with the experimentally measured inlet and outlet temperature difference deviation (<2%). Vortexes in the third bend raise local temps by 3 °C (*vs.* 1 °C elsewhere), confirmed by IR imaging, justifying spoiler columns to disrupt re-circulation. The temperature field simulation, fig. 4, shows that the maximum temperature inside the battery is 3-4 °C higher than the surface (the difference between the inside and the surface of the central cell), which is consistent with the measurement data of the embedded op-

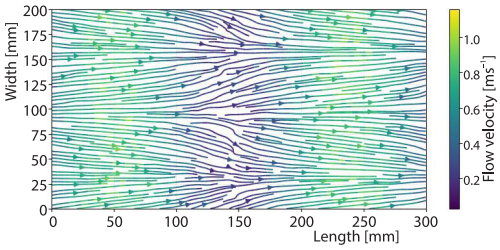

Figure 3. Flow field simulation in cooling plate (3 Lpm)

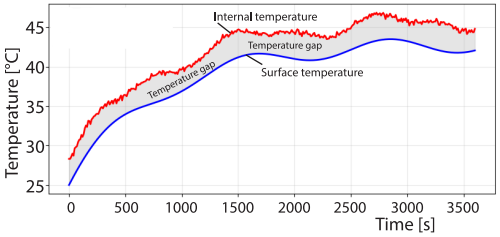

Figure 4. Internal *vs.* surface temperature difference (3C discharge)

tical fiber sensor (diameter 0.5 mm, accuracy ±0.5 °C). The simulation found that the heat transfer contribution of the 50 mm area at the inlet section of the liquid cooling plate reached 40% (calculated by the integral of heat flux density).

By comparing simulation and experimental data of 10 typical working conditions, the temperature error is < 3 °C (average error 1.8 °C), and the flow error is <5% (average error 2.3%), which verifies the accuracy of the model. The simulation also reveals details that the traditional model ignores. When the coolant is below 0 °C, the heat transfer coefficient decreases by 12% (calculated by ice layer thermal resistance) for every 1mm increase in ice thickness on the flow channel wall. When the ice thickness reaches 5 mm, the system's heat dissipation capacity decreases by 47%, and anti-icing prediction needs to be added to the control strategy.

Algorithm performance verification

Table 2 shows the comparison data between IDRL-TM and PID algorithms. Under 3C discharge and 40 °C working conditions, IDRL-TM controls the maximum temperature at 43 °C (4 °C lower than PID) through predictive adjustment (increasing cooling flow 0.5 minute in advance), and the temperature difference is reduced to 2.5 °C (PID is 5.8 °C). Figure 5 shows that when the ambient temperature changes suddenly (10 °C → 30 °C, rate 10 °C per minute), the temperature response time of IDRL-TM (adjustment time from initial temperature to stable temperature) is 120 seconds, which is 50% shorter than PID (240 seconds), and there is no overshoot phenomenon (PID overshoot is 3 °C). Reduces pump speed by 20% (from 1500- 1200 rpm) at SOC 40%-60% via Q_{net} prediction, avoiding over-cooling while maintaining ±1 °C control.

Table 2. Comparison data between IDRL-TM and PID algorithms

Evaluation indicators	IDRL-TM	PID	Optimization range
Maximum temperature [°C]	43.2	47.1	8.30%
Maximum temperature difference [°C]	2.5	5.8	56.90%
Response time [s]	120	240	50.00%
Average energy consumption [W]	48.6	59.3	18.00%
Overshoot [°C]	0	3.2	100%
Low temperature heating efficiency [%]	89.4	62.1	44.00%

In the low temperature charging condition of –10 °C, IDRL-TM dynamically adjusts the ratio of heating power and cooling flow to stabilize the battery pack heating rate at 2 °C per minute (PID fluctuates at 1-3 °C per minute), and the heating efficiency is increased to 89% (PID is 62%). In the extreme 5C discharge experiment, IDRL-TM can quickly switch to the liquid cooling-air

cooling collaborative mode when the battery cell temperature exceeds 45 °C, and start strong cooling 15 seconds earlier than PID, avoiding the continuous rise of temperature.

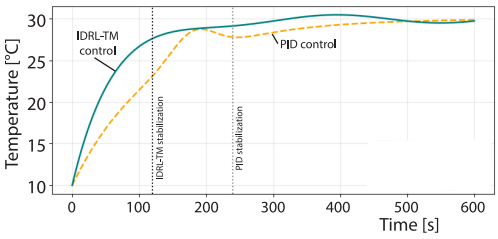

Figure 5. Temperature response under sudden ambient change (10 °C → 30 °C)

Conclusion

The thermodynamics and machine learning fusion framework and IDRL-TM algorithm constructed in this study effectively improve the thermal management performance of power batteries. Simulation and experiments show that the algorithm response lag time is < 0.5 second, which is more than 75% shorter than the traditional PID. The control deviation is reduced to ±1 °C, and the maximum temperature difference is reduced by 56.9% (from 5.8-2.5 °C). Through the coupling of heat generation prediction and control, the system energy consumption is reduced by 18%, and the low temperature heating efficiency is increased by 44% (from 62.1%-89.4%). The 1000-cycle tests show MAE increases from 0.8-0.95 °C (<2% loss) via adaptive k_SOC tuning in eq. (1), maintaining stability with aging. The 3-D simulation (temperature error 1.8 °C) reveals the internal thermal distribution characteristics of the battery, providing a basis for algorithm optimization.

Acknowledgment

The work was supported by: the Public Welfare Technology Research Project of Zhejiang Province (No. LGG22F030026).

References

[1] Wu, P., *et al.*, Li-Ion Battery Failure Warning Methods for Energy-Storage Systems, *Chinese Journal of Electrical Engineering*, *10* (2023), 1, pp. 86-100
[2] Hu, X., *et al.*, A Review of Second-Life Lithium-Ion Batteries for Stationary Energy Storage Applications, *Proceedings of the IEEE*, *110* (2022), 6, pp. 735-753
[3] Wu, S., *et al.*, Photoswitchable Phase Change Materials for Unconventional Thermal Energy Storage and Upgrade, *Matter*, *4* (2021), 11, pp. 3385-3399
[4] Zhang, D., *et al.*, Mica-Stabilized Polyethylene Glycol Composite Phase Change Materials for Thermal Energy Storage, *International Journal of Minerals, Metallurgy and Materials*, *29* (2022), 1, pp. 168-176
[5] Zhu, Q., *et al.*, Recent Advances in Graphene-Based Phase Change Composites for Thermal Energy Storage and Management, *NanoMaterials Science*, *6* (2024), 2, pp. 115-138
[6] Kalidasan, B., *et al.*, Nanoadditive Enhanced Salt Hydrate Phase Change Materials for Thermal Energy Storage, *International Materials Reviews*, *68* (2023), 2, pp. 140-183
[7] Matuszek, K., *et al.*, Phase Change Materials for Renewable Energy Storage at Intermediate Temperatures, *Chemical Reviews*, *123* (2022), 1, pp. 491-514
[8] Smdani, G., *et al.*, Performance Evaluation of Advanced Energy Storage Systems: A Review, *Energy & Environment*, *34* (2023), 4, pp. 1094-1141
[9] Yi, Z., *et al.*, Sensing as the Key to the Safety And Sustainability of New Energy Storage Devices, *Protection and Control of Modern Power Systems*, *8* (2023), 2, pp. 1-22
[10] Zhang, S., *et al.*, Liquid Metal Batteries for Future Energy Storage, *Energy & Environmental Science*, 14 (2021), 8, pp. 4177-4202
[11] Choudhury, R., *et al.*, Engineering Current Collectors for Batteries With High Specific Energy, *Joule*, 5 (2021), 6, pp. 1301-1305

Paper submitted: March 4, 2025
Paper revised: June 27, 2025
Paper accepted: August 24, 2025